Self-Assembly of Hierarchical High-χ Fluorinated Block Copolymers with an Orthogonal Smectic-within-Lamellae 3 nm Sub-Lattice and Vertical Surface Orientation

Bijal B. Patel[1‡], Hongbo Feng[2‡], Whitney S. Loo[3], Chad R. Snyder[1], Christopher Eom[2], Julia Murphy[1], Daniel F. Sunday[1,*], Paul F. Nealey[2,*], Dean M. DeLongchamp[1,*]

[1]*Material Measurement Laboratory, National Institute of Standards and Technology, Gaithersburg, MD 20899, USA*
[2]*Pritzker School of Molecular Engineering, University of Chicago, Chicago, IL 60637, USA*
[3]*Department of Chemical and Biological Engineering, University of Wisconsin—Madison, Madison, WI 53706, USA*

CORRESPONDING AUTHORS:

*dean.delongchamp@nist.gov, *nealey@uchicago.edu, *daniel.sunday@nist.gov

ABSTRACT: Hierarchical structure-within-structure assemblies offer a route towards increasingly complex and multifunctional materials while pushing the limits of block copolymer self-assembly. We present a detailed study of the self-assembly of a series of fluorinated high- χ block copolymers (BCPs) prepared via post-modification of a single poly(styrene)-block-poly(glycidyl methacrylate) (S-*b*-G) parent polymer with the fluorinated alkylthiol pendent groups containing 1, 6, or 8 fluorinated carbons (termed trifluoroethanethiol (TFET), perfluoro-octylthiol (PFOT), and perfluoro-decylthiol (PFDT), respectively). Bulk X-ray scattering of thermally annealed samples demonstrates hierarchical molecular assembly, with phase separation between the two blocks and within the fluorinated block. The degree of ordering within the fluorinated block is highly sensitive to synthetic variation; a lamellar sub-lattice was formed for S-*b*-GPFOT and S-*b*-GPFDT. Thermal analyses of S-*b*-GPFOT reveal that the fluorinated block exhibits liquid crystal-like ordering. The complex thin-film self-assembly behavior of an S-*b*-GPFOT polymer was investigated using real space (atomic force microscopy, scanning electron microscopy) and reciprocal-space (resonant soft X-ray scattering (RSoXS), grazing incidence small- and wide-angle scattering) measurements. After thermal annealing in nitrogen or vacuum, films thicker than 1.5 times the primary lattice spacing exhibit a 90-degree grain boundary, exposing a thin layer of vertical lamellae at the free interface, while exhibiting horizontal lamellae on the preferential (polystyrene brush) substrate. RSoXS measurements reveal the near-perfect orthogonality between the primary and sub-lattice orientation, demonstrating hierarchical patterning at the nanoscale.

KEYWORDS: Block Copolymer, thin film, hierarchical self-assembly, high-chi, Resonant Soft X-ray Scattering

Hierarchical materials comprise distinct structural motifs at multiple nested length scales, which collectively determine the resulting material properties.[1] This phenomenon underpins the extraordinary multifunctionality of biomaterials such as wood and bone, for which hierarchical growth from a limited set of elemental constituents enables simultaneous optimization of mechanical, transport, and stimuli-adaptive properties.[2] In recent decades, hierarchical design principles have been applied to improve performance for a wide variety of synthetic materials.[3] Although early examples focused primarily on mechanical properties,[4] more recent demonstrations target energy storage and conversion,[5,6] catalysis,[7,8] and stimuli-responsive 'smart' materials.[9]

Polymers provide an excellent platform for the design and optimization of synthetic hierarchical materials. Polymeric materials inherently exhibit

ordering across the molecular, nano-, micro- and macroscopic length scales,[10] described by characteristics such as regio- and stereochemistry, chain conformation, aggregation, degree and type of crystallinity, domain character (size, alignment, and orientation), and film morphology (*e.g.*, fibrillar, conformal, or porous). Mechanistically, polymer self-assembly often follows the same pathways that give rise to precise hierarchal ordering in nature: phase separation[11] and (conventional or liquid) crystallization.[12] With advances in polymer synthesis, an ever-growing library of architectures and backbone/side-chain constituents are now available as building blocks with specific targeted interactions, enabling hierarchy by design.[13–15] At the same time, intra- and inter-molecular forces can be tailored to be strong enough for bottom-up self-assembly processes, but weak enough to provide ready access to metastable microstructures, offering additional routes towards tuning performance under mild processing conditions.[13,16]

Block copolymers (BCPs) comprise chain segments that are covalently linked but chemically dissimilar. BCPs have been extensively studied as building blocks for well-controlled nanostructures with predictable length scales[13,17] in diverse applications such as nanopatterning[18–20] (nanolithography and porous templating), drug delivery,[21,22] and electronic/optical materials,[23–27] and have seen commercial success as adhesives, thermoplastic elastomers, and surfactants.[13] Historically, the most well-studied 'coil-coil' BCPs have been composed of topologically linear segments which adopt random chain conformations within amorphous microphase-separated domains. The equilibrium morphology of a coil-coil BCP is governed primarily by the relative volume fraction of each block; increasing asymmetry for a diblock BCP leads to a transition across lamellar, gyroid, cylindrical, and spherical geometries.[28] The driving force for microphase separation is described by the product of effective Flory-Huggins interaction parameter (χ) and the degree of polymerization (N), with microphase segregation occurring at $\chi N > 10.5$. In the strong segregation limit (SSL),[17] for coil-coil BCP, lamellar domain spacing (d) scales as $d \propto N^{2/3}\chi^{1/6}$. The most well-studied BCP applied to nanopatterning (poly(styrene)-b-poly(methyl methacrylate), PS-*b*-PMMA)) has been reported to have a limiting d of ≈22 nm.[29]

In this manuscript, we blend two key themes in ongoing research on BCPs: (1) studying an emerging class of 'high- χ' BCPs[30] with increasingly incompatible chemical constituents (for targeting smaller domain spacings), and (2) in developing hierarchical 'structure-within-structure' assemblies *via* incorporation of liquid crystalline (LC BCP) moieties, where the feature size of the LC phase typically extends down to (3 to 7) nm.[31] For both approaches, precise control over domain orientation is of critical importance in thin-film applications. For high- χ BCP, it can be challenging to achieve vertically oriented (substrate-perpendicular) domains, as the use of strongly dissimilar chemical constituents frequently leads to a substantial difference in surface energy between the blocks (which leads to the formation of substrate- and free interface-parallel structures). In such cases, achieving substrate-perpendicular domain orientation generally requires multi-step processing with the use of neutral substrate brushes and top-coats,[32,33] or careful selection of compatible chemistries with balanced surface energies.[34–36] By contrast, LC moieties can be exploited to promote substrate-perpendicular orientation as they exhibit strong and tunable anchoring tendencies with respect to the free interface and LC/BCP intermaterial dividing surface.[37–41]

A variety of high- χ BCPs with domain spacings approaching ≈10 nm have been reported.[30] Although silicon- and nitrogen- containing polymers such as poly(dimethyl siloxane) – *block* – poly(methyl methacrylate), PDMS-*b*-PMMA ($\chi \approx 0.2$ at 150°C)[42] and poly(styrene)-block-poly(4-vinylpyridine), PS-*b*-P4VP ($\chi \approx 0.317$ at 160°C)[43] have been demonstrated,[30] they frequently suffer from large kinetic barriers to long-range ordering and require long annealing times and/or expensive chemical templating. Reports describing the use of fluorine-containing moieties have highlighted the potential for achieving high- χ, small feature sizes, and rapid self-assembly, generally with substrate-directed control over domain orientation.[44–48] Jo, Ryu, *et al.*[46] synthesized poly(styrene)-*b*-poly(2,2,2-trifluoroethyl acrylate)s (PS-*b*-PTFEAs) with χ of 0.233 at 150 °C and formation

of substrate-perpendicular 10 nm lamellar domains in as-spun films deposited onto a neutral homopolymer mat at room temperature. Li, Deng, *et al*.[44] synthesized a series of poly(styrene)-*block*-poly(pentadecafluorooctyl methacrylate) (PS-*b*-PPDFMA) copolymers with χ of 0.353 at 150 °C that formed lamellar and cylindrical morphologies with domain spacing from (8.7 to 14.9) nm. They demonstrated formation of well-ordered domains after as little as 1 min of thermal annealing at 80 °C with a graphoepitaxial 'trench' template directing orientation. They attribute rapid ordering to high mobility and low coefficients of friction within the fluorinated block. The same group later synthesized poly(pentadecafluorooctyl methacrylate)-*block*-polyhydroxystyrene (PPDFMA-*b*-PHS) with χ of 0.48 at 150 °C and a d-spacing of 9.8 nm upon only 1 min of thermal annealing.[45] Yoshimura, Hayakawa *et al*.[36] designed a surface-energy balanced, singly fluorinated poly(styrene)-*block*-poly[2-hydroxy-3-(2,2,2trifluoroethylsulfanyl)propyl methacrylate (PS-b-PHFMA) with a χ of 0.191 at 25°C, capable of forming 9.6 nm spacing vertical lamellae on a random copolymer brush.

Prior investigations into LC-BCPs containing fluorinated moieties have revealed interesting multiscale orientation effects. Busch, Ober *et al*.[49] demonstrated that mesogenic tilt of semifluorianted alkyl side chains can propagate throughout the film thickness of a vertically oriented, cylinder-forming LC-BCP. Al-Hussein, de Jeu *et al*.[50] observed that anchoring of fluorinated side chains in poly(methyl methacrylate)-*b*-poly(1H,1H,2H,2H-perfluorodecyl acrylate) (PMMA-*b*-PF8H2A) at the air interface lead to stabilization of substrate-perpendicular cylinders and substrate-parallel lamellae. Recently, Dong, Hayakawa *et al*.[51] have demonstrated that tuning the composition of a substrate brush can effectively modulate orientation of fluorinated styrenic LC-BCPs.

In this work, we explore the self-assembly of a class of fluorinated styrenic block copolymers synthesized *via* thiol-epoxy "click" chemistry from a poly(styrene)-block-poly(glycidyl methacrylate) (S-*b*-G) parent polymer. X-ray scattering investigations of the bulk compounds demonstrate that the formation of hierarchical ordering is dependent on incorporation of a sufficiently long fluorinated moiety. We choose an LC BCP with intermediate fluorinated segment length for extensive thermal, real-space, and reciprocal-space characterization and demonstrate formation of an orthogonal smectic-within-lamellae hierarchical structure. The complex interplay between BCP and LC physics reveals itself in unexpected domain orientation behavior, as films which are thicker than the primary lattice spacing reorient during thermal annealing to form vertical lamellae at the free surface despite the apparent surface energy mismatch between the two blocks and the use of a strongly preferential substrate.

RESULTS AND DISCUSSION

Synthesis, Chemical Characterization and Self-Assembly in Bulk

Synthesis by post-modification of poly(styrene)-*b*-poly(glycidyl methacrylate) (S-*b*-G) was accomplished *via* a flexible thiol epoxy 'click' chemistry approach, chosen for its tolerance for a wide range of functionalities.[34,52,53] The resulting fluorinated polymers mirror those recently reported by Hayakawa *et al*. (aside from differing molecular weight).[36,51]

For initial characterization of bulk materials, a single batch of S-*b*-G was synthesized and used as the parent polymer for a series of three fluorinated BCPs with varying numbers of fluorinated carbons per repeat unit of the glycidyl methacrylate-derived block (**Figure 1a** and **Figure 1b**). We refer to these as S-*b*-GTFET (1 fluorinated carbon), S-*b*-GPFOT (6 fluorinated carbons), and S-*b*-GPFDT (8 fluorinated carbons), where TFET represents trifluoro-ethanethiol, PFOT represents perfluoro-octylthiol, and PFDT represents perfluorodecylthiol. Synthetic details and bulk materials properties are presented in **Table 1**. For later thin-film studies, a second (lamellar-forming) BCP (S-*b*-GPFOT2) was synthesized from a different parent S-*b*-G.

Table 1. Bulk Materials Properties of Synthesized Block copolymers

Name	N_{PS}	N_G	Đ (M_w/ M_n)	f_{PS}[a]	D_0 / L_0 (nm)[b]	D_s (nm)[b]	D_F (nm)[b]
S-*b*-G	87	59	1.02	0.45	13.2	-	-
S-*b*-GTFET	87	59	1.02	0.43	16.1	-	0.5
S-*b*-GPFOT	87	59	1.02	-	17.8	3.2	0.5
S-*b*-GPFDT	87	59	1.03	-	18.0	3.8	0.5
S-*b*-GPFOT2	109	30	1.03	0.44	24.2	3.2	0.5

[a] Estimated from peak intensity decay in the small-angle X-ray scattering (SI §3)[54]. [b] Calculated from transmission SAXS/WAXS experiments on bulk polymer films by dividing the position of the corresponding first order scattering peak (q*) from 2π.

Block copolymer self-assembly under equilibrium conditions was investigated by small- and wide-angle X-ray scattering (SAXS/WAXS, **Figure 1c**). Bulk (~mm thick) samples were thermally annealed at 150 °C for 20 h under vacuum prior to measurement. SAXS data are plotted for all four polymers in the initial series. For WAXS data, the parent polymer S-*b*-G showed no features as expected, so only the three derived BCPs are shown.

Bulk X-ray scattering data provide clear evidence of microphase separation between the styrene and glycidyl methacrylate-derived blocks through the position and intensity of the peaks in **I** vs **q** in the SAXS region[55] (numbered in black in **Figure 1c)**. The parent polymer (S-*b*-G), and the BCP with the shortest fluorinated chain (S-*b*-GTFET) are assigned as lamellar phases with SAXS peaks at q_n/q_1 = 1, 2, 3. S-*b*-GPFOT and S-*b*-GPFDT are more difficult to assign; the visible peaks at $q_n/q_1 = 1, \sqrt{3}, \sqrt{7}, \sqrt{9}, \sqrt{12}$ appear consistent with a hexagonally packed cylindrical phase (as others have observed for this chemistry,[51] although the peak at $q_n/q_1 = \sqrt{4}$ is absent. For later thin-film studies, an additional lamellar-forming BCP sample (S-*b*-GPFOT2) was synthesized from a different (more styrene-rich) parent S-*b*-G. Polystyrene volume fractions for lamellar-forming BCPs were estimated from the decay in integrated peak intensity with peak order[54] and range from (0.43 to 0.45), consistent with the conventional BCP phase diagram.[28]

The unit cell dimension is calculated as $D_0 = 2\pi/q^*$ (labeled as L_0 for lamellar phases and tabulated in **Table 1**). With increasing perfluorinated segment length, and accounting for the hcp geometry of S-*b*-GPFOT, and S-*b*-GPFDT, we observe a monotonic increase in the center-to-center distance between domains from 13.2 nm for the parent S-*b*-G to 16.1, 20.55, and 20.78 nm for S-*b*-GTFET, S-*b*-GPFOT, and S-*b*-GPFDT, respectively. The observed increase in center-to-center distance is qualitatively consistent with the increase in volume of the modified G block.

The bulk X-ray scattering data also indicate ordering within the glycidyl methacrylate-derived block. For S-*b*-GTFET, the single diffuse peak at $q \approx 7.0$ nm^{-1} may indicate weak organization, whereas for S-*b*-GPFOT (6 fluorinated carbons) and S-*b*-GPFDT (8 fluorinated carbons), there is a clear indication of an additional level of lamellar ordering, with sharp first-order peaks at $q \approx 2.0$ nm^{-1} and 1.65 nm^{-1}, respectively, and multiple visible peak orders at integer multiples in q (numbered in gold in **Figure 1c**). This ordered structure

within the glycidyl methacrylate-derived block is hereafter referred to as the 'sub-lattice', and described by unit cell dimension $D_{s,}$ with values of ≈ 3.15 nm and ≈ 3.8 nm for S-*b*-GPFOT and S-*b*-GPFDT, respectively.

The molecular packing within the sub-lattice can be inferred by comparing the measured D_s values to the spacing calculated assuming simple 'bilayer' packing within the fluorinated block (**SI §4,** illustrated within **Figure 1d**). The even-order sublattice scattering peaks of S-*b*-GPFOT are suppressed, indicating that the GMA-derived linker (low electron density) and perfluorinated segment (high electron density) occupy roughly the same volume in the sublattice unit cell. Hence each of the fluorinated domains has a thickness of $D_s/2$ ≈ 1.6 nm. Assuming the maximal extent of a 'bilayer' arrangement, where fluorinated chains enter the domain from either blue/green interface without interdigitation, a single fluorinated segment extends across $D_s/4$ ≈ 0.79 nm. Based on the tetrahedral bond angle of carbon at 109.5°, C-C bond length of 0.154 nm, and C-F bond length of 0.135 nm, we calculate the maximal extension of the fluorinated segment of S-*b*-GPFOT to be 0.739 nm (within ≈ 5.9% of the measured value). A similar analysis for the perfluorinated segment of S-*b*-GPFDT yields a measured value of ≈ 1.1 nm, while the calculated length is 0.991 nm (≈ 11.9% smaller). The molecular cartoon and scattering measurements are in good agreement and support the proposed 'bilayer' molecular conformation.

All fluorinated block polymers exhibit broad high-angle peaks in the WAXS data (**Figure 1c**) centered at $q \approx (12 \text{ to } 14)\ nm^{-1}$ ($D \approx (0.45 \text{ to } 0.52)$ nm), which we attribute to the interchain correlation (D_F) between perfluorinated segments. This measured spacing is in good agreement with the observed (100) spacing in crystalline hexagonally packed polytetrafluoroethylene (≈ 0.5 nm).[56] Given the layered nature of the sublattice and its weak degree of interchain order, we would tentatively classify the sublattice as a smectic-like liquid crystal; the thermal behavior of the BCP presented later robustly supports this classification.

From the data presented so far, BCP S-*b*-GPFOT2 forms a hierarchical structure comprising a primary lamellar S-*b*-G lattice, a lamellar sublattice within the PG-derived block, and molecular stacking between perfluorinated segments. Three possible cartoons of this nested structure are illustrated in **Figure 1d**. Of these, the first option (sublattice oriented parallel to primary lattice) can already be excluded based on the measured volume fraction (f_{PS}) values and the high degree of coherence in the sublattice peaks. Transmission measurements through bulk samples are unable to differentiate between options 2 and 3, because the relative orientation of the primary and sub-lattice is 'averaged out' when a population of randomly oriented grains are sampled by the beam. In a subsequent section of the results, we apply resonant soft X-ray scattering to an ultra-thin film (thickness ≈ 1.5 L_0) and demonstrate the orthogonality of the primary and sub-lattice (option 3).

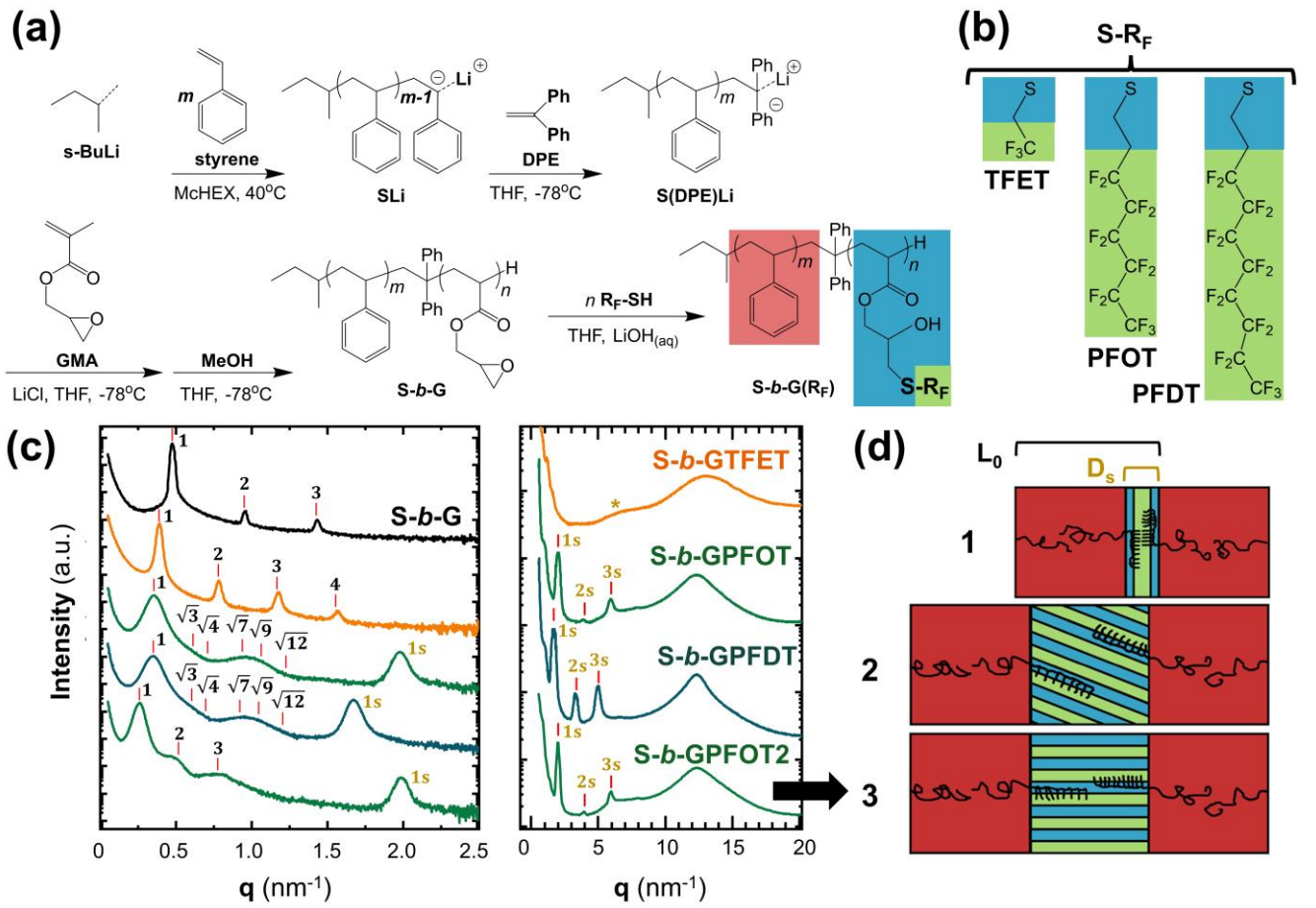

Figure 1. (a) Synthetic scheme for preparation of high-χ block copolymers and **(b)** series of fluorinated alkanethiols that were attached to the glycidyl methacrylate derived block. **(c)** Azimuthally averaged small- and wide-angle X-ray scattering profiles for parent polymer S-*b*-G, and block copolymers S-*b*-GTFET, S-*b*-GPFOT, and S-*b*-GPFDT, providing evidence of molecular assembly at three distinct length scales. Intensity is plotted on a log scale and shifted vertically for clarity. Peak orders of the primary lattice are numbered in black, while sub-lattice peaks are numbered in gold as 1s, 2s, *etc*. The single broad peak at $q \approx 12$ nm^{-1} ($D_F \approx 0.5$ nm) is attributed to the inter-chain packing within perfluorinated (green) regions. **(d)** Simplified cartoon of three possibilities for the primary/sublattice hierarchy that could form from the S-*b*-GPFOT2 block copolymer. We note that the structures (and especially polymer backbone) actually meander in 3-dimensions, not 2, as illustrated. Using resonant soft X-ray scattering (**Figure 4**), we demonstrate conclusively that structure 3 is obtained (perpendicular primary and sub-lattice orientation).

Thermal Characterization of Smectic-like Liquid Crystalline S-*b*-GPFOT2

Identifying the mesophase identity in polymeric systems poses a challenge due to the similarity between scattering patterns produced by 'classic' liquid crystalline phases, conformationally disordered ('condis') crystals, and polymer films exhibiting either low degrees of normal crystallinity or high degrees of orientational disorder. To differentiate between these options, we conducted a series of thermal measurements at different heating and cooling rates using conventional and Flash Differential Scanning Calorimetry (DSC) for polymer S-b-GPFOT2. We then applied the classification scheme proposed by Wunderlich *et al*. to the transition observed at > 180 °C. [57,58] We note that thermal degradation (non-recoverability of transition peaks) was apparent when heating above 180°C at 10°C/minute by conventional DSC, but not when using Flash DSC at 50 K/s, 100 K/s.

Upon cooling, we observe that the exothermic transition at ≈ 190 °C exhibits little or no cooling rate dependence (**Figure 2a)**, indicating the absence of a kinetically governed process (ruling out 'condis' and 'normal' crystals). Upon heating the sample to examine the corresponding "melting"/disordering process, we observe that peak melting temperature ($T_{m,p}$) depends on heating

rate (β) in agreement with the superheating equation: [59]

$$T_{m,p} = T_{m,0} + A\beta^{z} \quad (1)$$

(where A and z are fit constants). This indicates that the shifting onset of the melting transition is dominated by heat diffusion effects. Applying equation 1 to extrapolate to zero heating rate (**Figure 2b)**, we find a peak endothermic transition temperature of $T_{m,0} = (192.7 \pm 0.4)$ °C.

The minimal (<< 10 K) undercooling for the transition suggests that the transition is thermodynamically reversible and occurs without requiring nucleation and hence indicates a liquid crystalline mesophase transition. The bulk scattering data indicate the formation of lamellar ordering within the sub-lattice, so we classify the structure as 'smectic-like' liquid crystalline order.

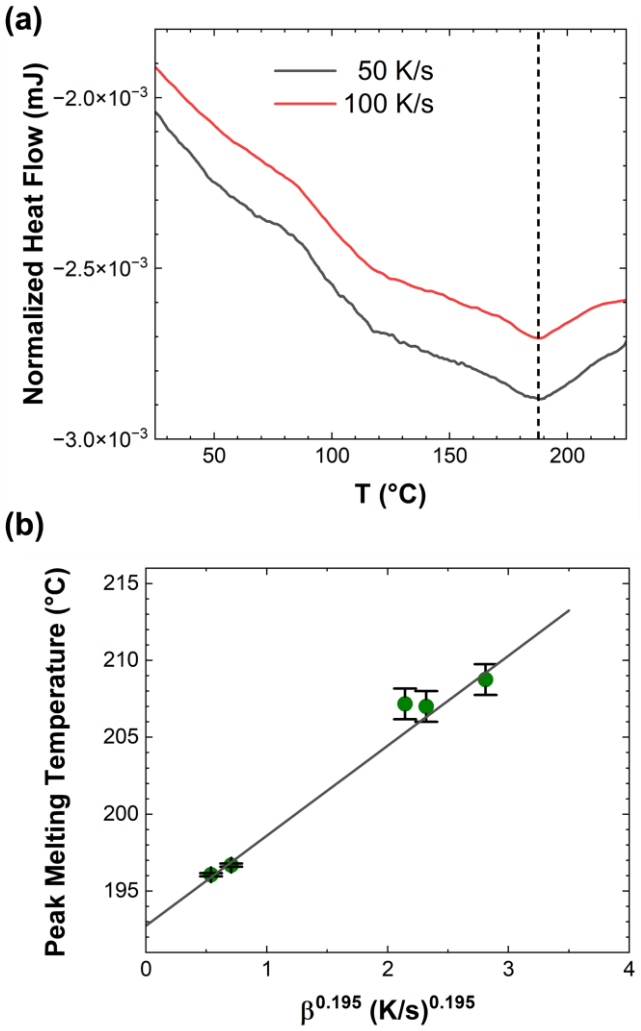

Figure 2. (a) Ultrafast DSC cooling traces at rates of -50 K/s and -75 K/s. (b) Peak melting temperature $T_{m,p}$ as a function of heating rate β from both standard and ultrafast DSC measurements. Line is a fit to the superheating equation (equation 1). Error bars are the best estimate of one standard deviation in the experimental uncertainty.

Thin Film Processing and Real-Space Characterization

Having developed an understanding of the bulk behavior of these materials, we will shift into interrogating the thin film behavior. A lamellar-forming BCP containing the medium-length perfluorinated segment (S-*b*-GPFOT2) was chosen due to its clear multiscale self-assembly at lower sub-lattice pitch than the GPFDT, and its presumed higher molecular mobility due to its lower melting point. Initial attempts at solution-casting films from tetrahydrofuran onto either bare silicon or PS-brushes resulted in the formation of unusual multilayered terraces with incomplete surface coverage (**Figure S17**). To produce smooth films suitable for X-ray characterization, we switched to spin coating from a mixture of toluene and trifluorotoluene and obtained films with thicknesses ranging from ≈ (0.5 L_0 to 4 L_0) on PS-brush-coated Si.

Atomic force microscopy (AFM) was used to investigate the degree of self-assembly and surface orientation of the primary lattice before and after annealing for 3 h under vacuum at 150 °C with slow cooling overnight. As-cast films were featureless (**Figure 3j**). The AFM images of annealed films prepared at 0.5 L_0 showed no evidence of vertical lamellae at the primary lattice spacing (**Figure 3a**), whereas the top surface of all annealed films prepared at thicknesses greater than 1.5 L_0 exhibited vertical lamellae (**Figure 3b,c,d**). For all incommensurate films (prepared at thicknesses which were not at integer multiples of half the primary lattice dimension), the vertical lamellae appeared within film height fluctuations that are consistent with island-hole behavior for BCPs between a preferential substrate and neutral free interface[60]. Annealing at elevated temperature and for extended periods (180 °C for 24 hours) led to thermal degradation of the film consistent with observations from DSC.

Scanning electron microscopy (SEM) cross-sections of films prepared at 1.5 L_0 and 3.2 L_0 thicknesses (**Figure 3m, S15**) provide evidence for two visually distinct layers, comprising vertically oriented domains at the free interface which then transitions to a different buried morphology. Films were ultraviolet (UV)-crosslinked to reduce distortions to film structure during cleaving. Further investigation of the out-of-plane structure of these films by grazing incidence X-ray scattering supports the interpretation of the buried layers as horizontal lamellae. For the thinnest films (0.5 L_0) resonant soft X-ray scattering (RSoXS) was used to determine that the top surface exhibited the vertically oriented sub-lattice, with the total film thickness consistent with the presence of a single molecular layer. From these results, we construct a series of morphological cartoons (**Figure 3e-f**) that require a 90° grain boundary of the primary lattice buried within the film.

The vertical orientation of the primary lattice domains at the top surface of the film is unusual and runs counter to the behavior of well-studied coil-coil BCPs, which require nearly equal surface energies between blocks. Based on the large surface energy difference between semi-fluorinated chains (23.1 mJ/m^2)[51] and polystyrene (40.7 mJ/m^2),[61] we would anticipate an asymmetric wetting condition[33], where the primary lattice would adopt substrate-parallel (horizontal) orientation throughout the entire film regardless of film thicknesses. The anchoring tendency of the LC-block provides a likely explanation of the observed behavior. Substrate-parallel orientation of the primary lattice allows for simultaneous homeotropic orientation of the fluorinated chains (extending into the free interface) and homogeneous orientation with intermaterial dividing surface between blocks.[40,50]

The long-range ordering behavior of this family of fluorinated BCPs also appears to differ from that of a coil-coil lamellar BCP. In a coil-coil lamellar film, the grains develop locally, with progressive alignment of the lamellae and annihilation of defects as small grains merge. Ordering on larger scales only occurs after very long times or under the influence of an external field. For the BCPs studied here, mild annealing conditions resulted in long range orientational correlations that exist on the mm scale (**Figure 3k, S14, S16**), however locally the film remains highly defective. We speculate that this behavior is related to the liquid crystalline character of the fluorinated groups; LC systems often exhibit long-range ordering and vertical alignment[41,50]. These findings add to a growing body of literature demonstrating rapid and/or highly long-range ordering in fluorinated BCPs, although the exact mechanism merits further study.[36,44–46]

Although, the (≈ 3 nm) sub-lattice was too small to directly visualize, the AFM images provide evidence of variation in sub-lattice orientation at the free interface. Across all AFM images with vertical primary lamellae, dark/soft spots in the phase consistently appeared and were confined within one set of domains. These do not appear to arise from measurement artifacts; their position and appearance is unchanged upon varying scan direction or cantilever setpoints (tapping force) (**Figures S11 – S13**). We suspect that they could arise from horizontally-oriented regions of the sub-lattice amidst a primarily vertically-oriented population (depicted in **Figure 3f,g,h**). This hypothesis is supported by the grazing incidence scattering data discussed later and by the lack of such spots in the AFM of the 0.5 L_0 thickness film (where the sub-lattice is geometrically constrained to vertical orientation).

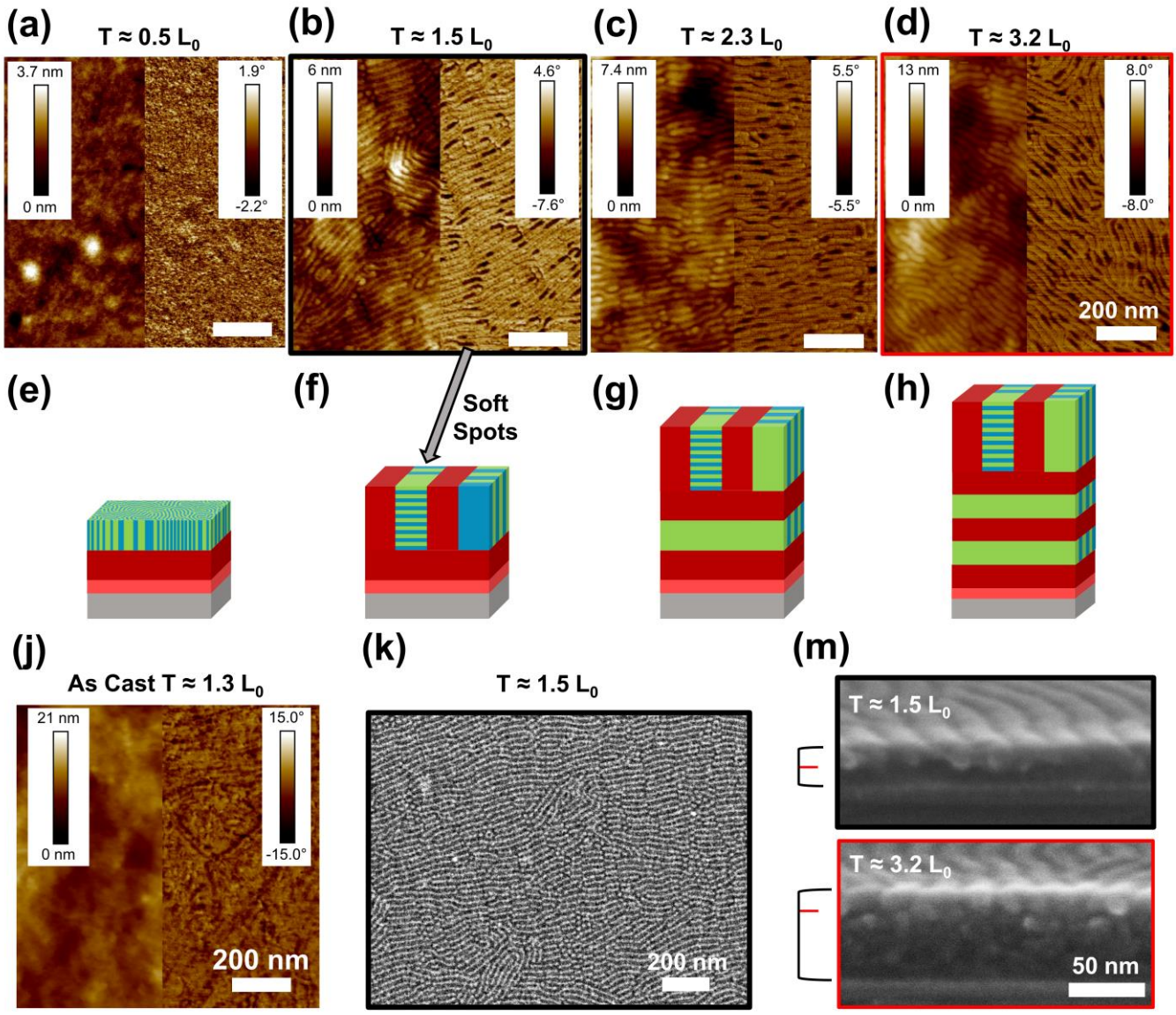

Figure 3. (a-d) Atomic Force Microscope (AFM) tapping-mode height (left) and phase (right) images for films of S-*b*-GPFOT2 spin cast from 0.5 mass ratio toluene/ α-α-α-trifluorotoluene and annealed at 150 ℃ for 3 h under vacuum. Images are presented as two halves of the same measurement for ease of visual comparison of height and phase (*i.e.*, the left side of each scan-line is shown in height, and the right side in phase). Scale bars represent 200 nm. Film thicknesses measured by variable angle spectroscopic ellipsometry are labeled above as multiples of the 24.4 nm bulk lattice period L_0. (e-j) Cartoons of thin-film morphology of annealed films of S-*b*-GPFOT at thicknesses corresponding to labels in **(a-d). (j)** AFM tapping-mode height (left) and phase (right) images for an as-cast film of S-*b*-GPFOT2 BCP. **(k)** Top-down scanning electron microscopy (SEM) image of an annealed film of S-*b*-GPFOT2 prepared at a thickness of approximately 1.5 L_0. Contrast was achieved *via* 2 cycles of sequential infiltration synthesis of alumina (AlO_x). Scale bar represents 200 nm. **(m)** Cross-sectional SEM images of annealed, Ultraviolet light (UV)-crosslinked films at thicknesses of 1.5 L_0 (above) and 3.2 L_0 (below). Annotation at left indicates the top and bottom of the film (black) and approximate edge of the vertically oriented surface layer (red). Scale bars represent 50 nm.

In-Plane Primary/Sub-Lattice Orientation by Resonant Soft X-ray Scattering (RSoXS)

The measurements discussed thus far have clarified the orientation of the primary lattice at the top surface, however these measurements have been insensitive to the orientation distribution of the fluorinated sublattice with respect to the primary lattice. To determine this, RSoXS measurements

were collected for annealed samples of S-*b*-GPFOT2 prepared at thicknesses of approximately 1.5 L_0 (**Figure 4a-d)** and 0.5 L_0 (**Figure 4e-g)**. Samples were prepared analogously to the previous thin-film measurements, other than the use of back-etched silicon nitride (with PS-brush) as the substrate. Measurements were taken in transmission mode at normal incidence and directly probe the in-plane film structure.

The RSoXS measurement is conceptually a combination of X-ray scattering and X-ray spectroscopy.[62] Here we present data collected near the Fluorine absorption edge (**Figure 4a)**, which dramatically increases scattering contrast and allows for clear scattering features even with ultra-thin films (here as low as 12.5 nm, **Figure 4e**). For both sets of RSoXS data discussed here, beam polarization effects were observed, indicating the presence of molecular orientation (**Figure S18, S19**). Modeling the presence and extent of molecular orientation within the BCP domains is beyond the scope of this manuscript and is the subject of ongoing study. Instead, these effects were minimized averaging scattering data collected at 0° and 90° polarization for the following analysis. An extended discussion of relevant fundamental and measurement details of RSoXS is provided in the supporting information. [63,64]

The two-dimensional scattering data for the 1.5 L_0 film (**Figure 4b**) provides a clear demonstration of the orthogonality of the primary and sub-lattice orientations. Azimuthal integration to generate 1D scattering traces (**Figure 4c**) confirms that the inner set of peaks (at $q < 1.2$ nm^{-1}) correspond to the primary lattice spacing of $L_0 \approx 24.4$ nm, while the outer peak at $q \approx 2.0$ nm^{-1} ($D_s \approx 3.2$ nm) corresponds to the sub-lattice. The relative angular distribution of the domains was measured quantitively by integrating azimuthal wedges that encompass the primary (black) and sub-lattice (blue) peaks (**Figure 4d**). The difference in azimuthal peak position was calculated to be 89.2°, reflecting the near perfect orthogonality of the primary and sub-lattice (as depicted in the cartoons of **Figure 3f, and option 3 of Figure 1d**). The strong degree of biaxiality encountered in this RSoXS measurement suggests only one or few grain orientations within the nominal RSoXS beam size of ≈ (250 μm x 250 μm). This assessment is supported by the results of an RSoXS spatial survey scan across the film which revealed mm-scale orientational correlations (**Figure S16**)

RSoXS data for the 0.5 L_0 film (**Figure 4e**), suggests isotropic in-plane orientation of the sub-lattice, and no in-plane organization of the primary lattice, as evidenced by the isotropic ring in the polarization-averaged 2D scattering data at $q \approx 2.0$ nm^{-1} (azimuthal linecut shown in (**Figure 4g**). This is consistent with the structural cartoon in **Figure 3e** and the AFM in **Figure 3a**. At this film thickness, there is only a single molecular layer present, with the PS domain anchored by the PS-brush at the substrate interface. Thus, the primary lattice is oriented out-of-plane and the in-plane orientation of the sub-lattice is left unconstrained.

We make two additional observations from the RSoXS data. First, the azimuthally averaged data (**Figure 4f**), reveals a noticeable splitting of the sub-lattice peak in both films, with peaks corresponding to $D_s \approx 3.16$ nm and $D_s \approx 3.07$ nm. These may suggest formation of a subtle polymorph of the lattice. Second, for the 0.5 L_0 film, there is a peak of unclear origin at $q^* \approx 0.6$ nm^{-1}, with no corresponding ≈ 10 nm periodicity apparent in the AFM data. There are many possible origins of this feature, including composition, roughness, or orientational heterogeneities; we aim to deconvolute these *via* ongoing simulation work.[64,65]

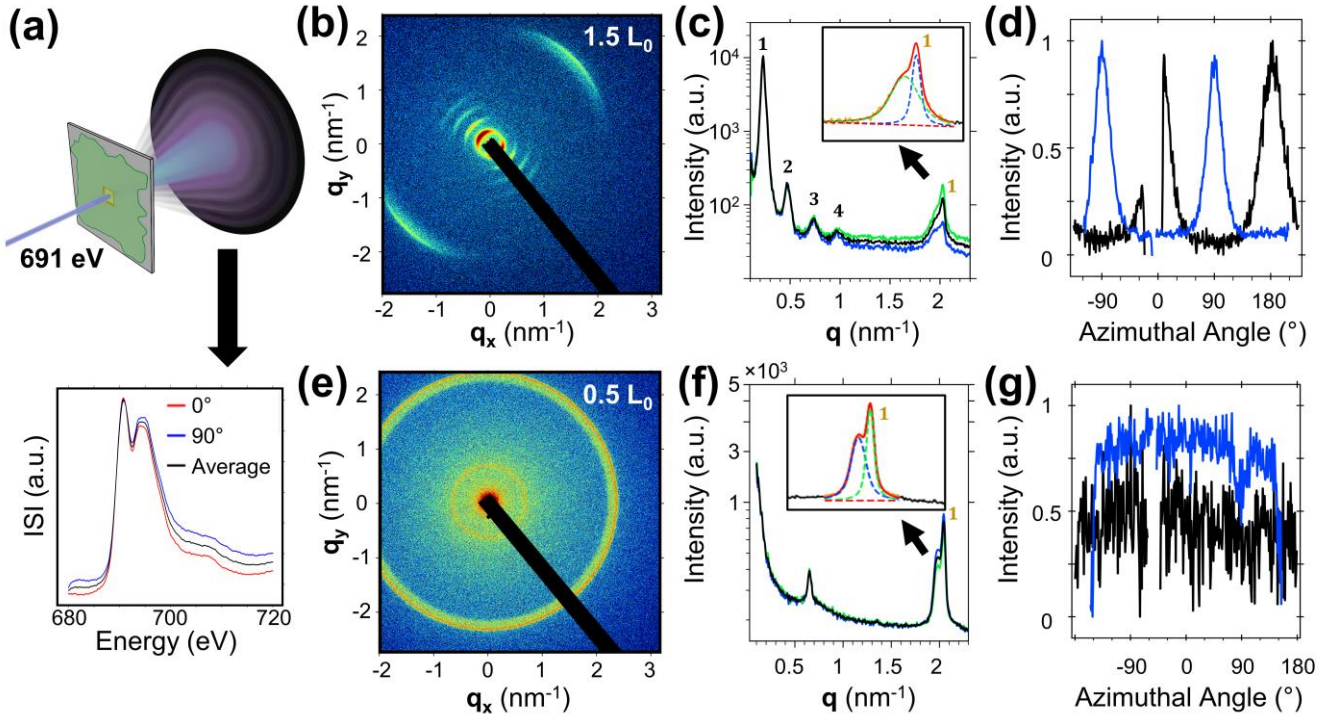

Figure 4. Resonant Soft X-ray Scattering (RSoXS) data collected from films of S-*b*-GPFOT2 spin cast from toluene/trifluorotoluene and annealed at 150 °C for 3 h. **(a)** Cartoon of the RSoXS measurement geometry and the azimuthally integrated scattering intensity (ISI) computed for a series of scans across the Fluorine absorption edge for a film with thickness 1.5 L_0. Beam polarization is noted in the figure legend. In (**b-g**), (**b,c,d**) are data collected for a film with thickness 1.5 L_0, while (**e,f,g**) are for a film with thickness 0.5 L_0. **(b,e)** 2D Resonant Soft X-ray Scattering pattern taken at 690.75 eV and averaged between scans taken at 0° and 90° beam polarizations to reduce molecular orientation effects. **(c,f)** Main panel: Azimuthally integrated scattering data collected at 0° (blue), 90° (green) polarization and their average (black). Black numbering indicates peak orders of the primary lattice. Gold numbering indicates first order peak of the sub-lattice. Inset: deconvolution of the primary fluorinated sub-lattice peak at ≈ 2.0 nm^{-1}. **(d,g)** Azimuthal linecuts integrated over q = (0.55, 0.80) nm^{-1} (black trace) and q = (1.9, 2.1) nm^{-1} (blue trace) normalized against their minimum and maximum values.

In- and Out-of-Plane Orientation by GISAXS/GIWAXS

Grazing incidence small-angle and wide-angle X-ray scattering (GISAXS/GIWAXS) measurements provide a statistically significant nanoprobe for thin-film structure that corroborates the real-space imaging data discussed prior. In this section, we discuss the results of synchrotron GISAXS/GIWAXS measurements for a series of films of S-*b*-GPFOT prepared by spin-coating as thin films onto PS-brush coated silicon wafers at thicknesses of approximately 1.3 L_0, 2.3 L_0, and 4 L_0. Data measured at an incident angle (α_i) of 0.11° are presented in **Figure 5** (GISAXS, **Figure 5a,b,c** ; GIWAXS, **Figure 5d,e,f**), with the full dataset presented in **Figure S20**.

An initial point of study is to examine the effect of the thin-film geometry on the characteristic size scales of each level of hierarchical structure to gauge the influence of confinement effects. We first consider the in-plane structure for all three films as compared with the behavior of the bulk BCP by plotting horizontal linecuts (**Figure 5g**) taken at q_z just above the horizontal stripe of enhanced intensity at the Yoneda band. Aside from geometry correction at high angles, the in-plane scattering in grazing incidence measurements can be interpreted in the same manner as the transmission measurements of the bulk materials. We observe no major differences in peak position (domain size), number, or shape between the bulk and thin-film samples or within the thin-film series. These observations are consistent with the real-space imaging data: that there is a layer of substrate-perpendicular primary lamella covering the top surface of every film. It is unsurprising that unit cell dimensions are unchanged versus the bulk sample, since the lateral (in-plane) dimension of the film is unconfined.

The scattering data also support the assertion that for films thicker than 1.5 L_0, there are two distinct orientations of the sub-lattice: parallel and perpendicular to the substrate. This is evident in the GIWAXS data (**Figure 5d,e,f**) by examining an azimuthal arc extending from $q_z \approx 6\ nm^{-1}$ to $q_r \approx 6\ nm^{-1}$ (encompassing the third order sub-lattice stacking peak). The sharp increases in intensity in the narrow regions around the q_z and q_r axes indicate that there are two distinct (and narrowly distributed) populations of substrate-parallel and substrate-perpendicular sub-lattice orientations. These data support the interpretation of the 'soft spots' in the AFM phase image discussed prior.

The out-of-plane (substrate-perpendicular) ordering of the primary lattice is investigated by examining vertical linecuts (along q_z) in the GISAXS pattern near the beamstop ($q_y = 0$) (**Figure S21)**. In the dynamical regime (where the incident angle exceeds the critical angle of the film), refraction and reflection of the incident and outgoing wave lead to a characteristic doubling of lamellar stacking peaks, as seen in **Figure 5h**, showing the incident-angle dependent linecuts for the film with thickness 4 L_0. Using the distorted wave born approximation (DWBA)[66–68], we compute a primary lattice spacing of $L_{0,parallel} \approx 25.2$ nm and a critical angle of 0.100°. There is also good visual agreement for the calculated positions for the first three sets of peaks (indicated in **Figure 5h**) Applying the same analysis for the 2.3 L_0 film yields L_0, parallel ≈ 23.7 nm. This values are only mild deviations from the bulk L_0 of ≈ 24.4 nm and can be explained by the incommensurability of film thickness and domain spacing.[33] The thinnest film (1.3L_0) did not have apparent peaks corresponding to a lattice of substrate-parallel lamellae. These results are consistent with the cartoons proposed in Figure 3**f,g,h**; as film thickness increases, additional substrate-parallel lamellae are incorporated below a layer of substrate-perpendicular lamellae.

The azimuthal orientation distribution of the fluorinated interchain stacking feature (perpendicular to the C-C chain direction) is probed by the distribution of scattering intensity around $q \approx 12.5\ nm^{-1}$. Qualitatively, we observe scattering intensity distributed broadly across azimuthal angle (χ), with enhanced scattering approaching the vertical direction ($\chi = 0°$). Local background-subtracted integrated intensity as a function of azimuthal angle is presented in **Figure 5j** before and after correction for the tilt of the Ewald sphere[69,70]. Comparison of the corrected signal to the isotropic baseline indicates that the interchain correlation is primarily isotropic (blue shaded region), with a minority population oriented in the vertical direction (purple shaded region).

These data are consistent with the observed bimodal sub-lattice orientation distribution. When the sub-lattice is oriented horizontally, the fluorinated chain backbones are stretched in-plane and the inter-chain correlation direction can be in any out-of-plane direction from $\chi = 0°$ to 90°. The weak observed bias towards $\chi = 0°$ could arise from surface templating effects. Conversely, when the sub-lattice is oriented vertically, the fluorinated chain backbones are stretched out-of-plane and the interchain correlation should be strictly in-plane ($\chi = 90°$). Unfortunately, resonance enhancement in the limit of $\chi \approx 90$ (Yoneda region) precludes definitive interpretation of the sharp peak at the horizon. Rigorously determining orientation distributions relative to the lamellar interface *via* polarized RSoXS experiment and simulation is an ongoing project of our group.

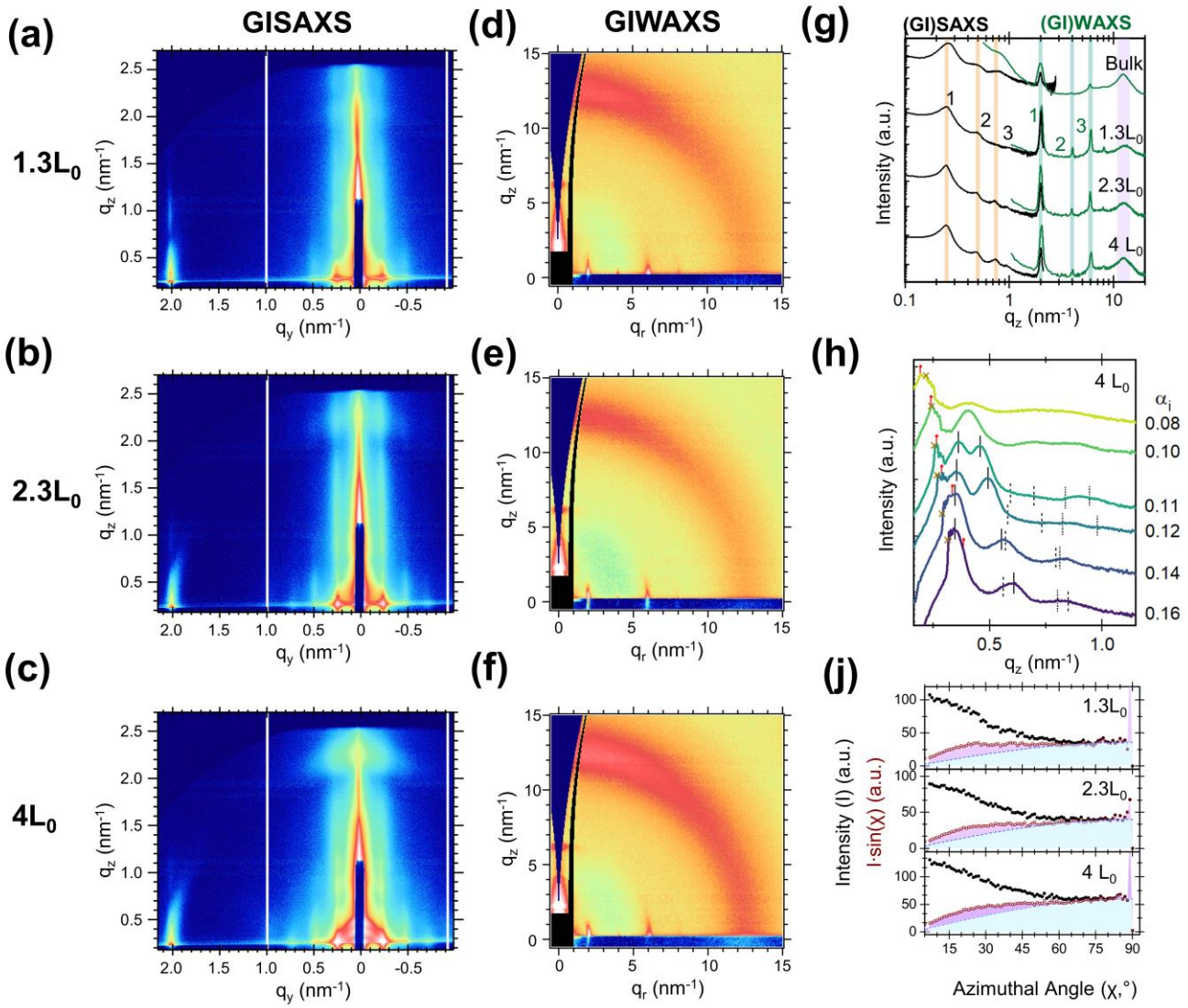

Figure 5. Grazing Incidence Small-Angle and Wide-Angle X-ray Scattering (GISAXS/GIWAXS) data collected from films of S-*b*-GPFOT2 spin cast from toluene/trifluorotoluene and annealed at 150 °C for 3 h. **(a-c)** 2D GISAXS and **(d-f)** reshaped GIWAXS data taken at an incident angle of 0.11° and beam energy of 13.5 keV from films of thickness 1.3L_0, 2.3L_0, and 4 L_0. (**g**) Comparison of scattering data for bulk and thin-film samples. Transmission SAXS/WAXS for the bulk S-*b*-GPFOT2 sample are plotted above, followed by GISAXS/GIWAXS horizontal linecuts calculated from the data in (**a-f**). Linecuts are taken just above the Yoneda and are plotted with respect to q_y for GISAXS data and q_r for GIWAXS data. (**h**) A series of vertical linecuts taken from GISAXS data from a film of thickness 4 L_0 at varying incident angle (α_i) as marked. The calculated position of the Yoneda peak (at exit angle α_f equal to the critical angle α_c) is marked with a gold 'x'. The calculated position of the specular beam is marked in red. Best-fit positions calculated for the two branches of the out-of-plane lamellar stacking peak (substrate-parallel primary lattice lamellae) are marked with solid lines (first order), dashed lines (second order) and dotted lines (third order). (**j**) Integrated intensity taken over an azimuthal wedge in the GIWAXS (with local background subtraction) encompassing the high-q interchain fluorinated correlation peak centered at ≈12.5 nm^{-1}. We define $\chi = 0$ along the q_z axis and χ =90 along the q_r axis. Filled black circles represent the raw integrated intensity, while open red circles include the sin(χ) correction factor for the tilt of the Ewald sphere. The dashed blue line corresponds to the isotropic baseline, allowing the purple and blue shaded regions to be interpreted as population fractions of oriented and isotropic chains.[69,70]

CONCLUSIONS

In this work, we study the self-assembly of a series of fluorinated block copolymers prepared *via* thiol-epoxy 'click' reaction of fluorinated alkylthiols (1, 4, and 6 fluorinated carbons) with a styrene-b-glycidyl(methacrylate) parent polymer. Upon

thermal annealing of bulk samples, hierarchical ordering is observed for the polymers with larger fluorinated moieties [S-b-GPFOT (6 fluorinated carbons), and S-b-GPFDT (8 fluorinated carbons)], with the degree of order within the fluorinated domain increasing as the perfluorinated segment length increases. Thermal analysis of a more symmetric polymer with 6 fluorinated carbons, S-b-GPFOT2 provides a clear indication of liquid crystal-like ordering within the fluorinated sublattice.

A detailed study of the thin-film structure of S-*b*-GPFOT2 reveals formation of a nested smectic-within-lamellar structure with near-perfect orthogonality between the primary lattice and sub-lattice. The complex thermodynamics of hierarchical ordering with a liquid-crystalline material also gives rise to several atypical self-assembly characteristics. We observe formation of a 90-degree grain boundary in the out-of-plane (film thickness) direction for film thicknesses greater than or equal to 1.5 times the primary lattice spacing (regardless of commensurability). Despite the high surface energy difference between the fluorinated and polystyrene domain, thermal annealing consistently results in the horizontal orientation of the primary lamellae at the styrene-brush substrate to give way to a layer of vertical lamellae at the free interface. These vertical domains also exhibit a high degree of orientational correlation (over the mm scale) over relatively short annealing times.

Further directions may take advantage of this type of self-assembly to additively fabricate complex architectures through a combination of a judicious choice of chemistries combined with sequential infusion synthesis to tune the desired properties of each component. One of the most intriguing features of this system is how the combination of LC physics and BCP self-assembly lead to unexpected behaviors. This includes the vertical orientation in films > 1.5 L0 in spite of the surface energy difference between the two components and the long range orientational order of the larger lattice feature in absence of any external field. Frequently, demonstrations of long-range organization on these multi-micron length scales require either a template or an external directing field. Given the degree of alignment that arises without a director, this system has the potential for even more rapid assembly if provided an external stimulus. These exciting developments provide guidance for developing materials for nanofabrication that take advantage of materials physics at multiple length scales.

METHODS

Extended Characterization Methods are provided in SI §1.[64,66,68,71–76]

Polymer Synthesis and Characterization

Reagents were sourced as follows: Styrene (S, 99%, Aldrich), glycidyl methacrylate (GMA, 99%, Aldrich), *sec*-butyllithium (*sec*-BuLi, 1.4 mol/L, Aldrich), 1,1-diphenylethylene (DPE, 97%, Aldrich), lithium chloride (LiCl, 99.95%, Aldrich), tetrahydrofuran (THF, 99.9%, Fisher Chemical), methylcyclohexane (McHEX, 99%, Aldrich), methanol (MeOH, 99%, Fisher Chemical), 2,2,2-trifluoroethanethiol (TFET, 95%, Aldrich), 1H,1H,2H,2H-perfluorooctanethiol (PFOT, 97%, Syn Quest Labs), 1H,1H,2H,2H-perfluorodecanethiol (PFDT, 97%, Aldrich).

Homopolymer poly(glycidyl methacrylate) (G) and BCP poly(styrene)-*b*-poly(glycidyl methacrylate) (S-*b*-G) were synthesized *via* living anionic polymerization and Schlenk techniques as reported previously.[34] An example synthesis of S-*b*-G is described below. To a five-neck anionic reactor was added McHEX (60 mL) followed by S (11.6 mL, 100.8 mmol). A gas-tight syringe was used to add 1.2 mL of *sec*-BuLi solution (1.4 mol/L) to the reaction mixture. The color of the mixture turned from colorless to orange, a characteristic color of the living anionic polymerization of S. The reaction mixture was stirred for 4 h at 40 °C. An aliquot of living S solution was taken using a gas-tight syringe and precipitated into degassed MeOH. The obtained homopolymer S was characterized by size exclusion chromatography (SEC) to obtain the number-averaged relative molecular mass (M_n) and dispersity ($Đ$) of the first block. To the mixture was added 2 mL of DPE (4 equiv) and the mixture was stirred for 15 min. The reactor was then slowly cooled to −78 °C followed by the addition of THF (250 mL) and LiCl (712 mg, 10 equiv) and stirred for 35 min to

ensure thermal equilibration. The desired amount of GMA (11.1 mL, 4.23 mol/L, 47.1 mmol in one example) in THF was then added to the mixture and stirred for another 30 min. Upon the addition of GMA monomers, the color of the solution turned from dark red to colorless. After 30 min, to the reaction mixture was added degassed methanol (3 mL), which terminated polymerization. The reaction mixture was then warmed to room temperature, concentrated, precipitated from hexanes twice, and dried in a vacuum oven at 40 °C.

A typical thiol-epoxy "click" reaction proceeded as follows. Approximately 100 mg of the S-*b*-G parent polymer (GMA mass fraction of 0.353, 0.252 mmol epoxy groups) was weighed into a 20 mL glass vial, and THF (≈3 mL) was added. To this, an excess amount of TFET (40 μL, 0.448 mmol, 1.78 eq) was added *via* a syringe. A magnetic stir bar was added, and the vial was placed in an ice bath to cool to 0 °C. A pre-chilled aqueous solution of LiOH (≈30 mg of a 20 mg mL^{-1} solution, 0.1 eq LiOH per epoxy group) was added to the cooled reaction mixture. The solution was allowed to warm to room temperature and then stirred for 24 h. The polymer was isolated by three precipitation cycles into hexanes from THF and dried in a vacuum oven overnight. Proton nuclear magnetic resonance (^{1}H-NMR) and size exclusion chromatography (SEC) data are provided in **SI §1**.

Thin Film Preparation

Silicon substrates (native oxide, University Wafer #452) were cleaned by UV-Ozone treatment for 10 min (Jelight Company UVO Cleaner Model No.42) before spin coating of a solution of polystyrene brushes (Polymer Source, Inc P11116-SOH, 6 kg/mol) prepared at a polymer mass fraction of 0.02 in Toluene (≥ 99.5%, Sigma-Aldrich). Coated wafers were annealed at 230 °C under nitrogen for greater than 24 h before three cycles of soaking in fresh propylene glycol monomethyl ether acetate (PGMEA, ≥ 99.5%, Sigma-Aldrich) for 3 h in a covered glass dish at 90 °C before a final soak for at least 12 h to remove unreacted brushes. Polystyrene brush film thickness was verified by variable angle spectroscopic ellipsometry.

All films presented in the main text were prepared by spin coating from solutions with polymer mass fraction of ≈ 0.02 in a 1:1 mass ratio mixture of toluene (≥ 99.5%, Sigma-Aldrich) and α-α-α-trifluorotoluene (≥ 99%, Sigma-Aldrich). Solutions were heated to 60 °C overnight to obtain transparent solutions and re-heated between spin coating to avoid clouding of the solution (which began within minutes upon cooling to room temperature). Films were spin coated at speeds ranging from (209 to 838) rad/s [(2000 to 8000) rpm]. and film thickness was checked using variable angle spectroscopic ellipsometry. All data in the main text are from films that were thermally annealed under vacuum at 150 °C for 3 h followed by slowly cooling overnight.

ASSOCIATED CONTENT

Supporting Information.

Extended synthesis and methods, thermal analysis, volume fraction estimation from small-angle X-ray scattering, geometric calculation of sub-lattice spacing, atomic force microscopy study of soft spots in phase, additional scanning electron micrographs of block copolymer thin films, resonant soft X-ray scattering spatial survey scan, additional thin-film processing results, polarization-dependent resonant soft X-ray scattering data, grazing incidence small- and wide-angle X-ray scattering data, supplemental references.

AUTHOR INFORMATION

Corresponding Author

*dean.delongchamp@nist.gov
*nealey@uchicago.edu
*daniel.sunday@nist.gov

Author Contributions

The manuscript was written through contributions of all authors. All authors have given approval to the final version of the manuscript.
‡These authors contributed equally.

ACKNOWLEDGMENT

B. Patel acknowledges the support of a NIST-National Research Council postdoctoral fellowship. Work at the Molecular Foundry was supported by the Office of Science, Office of Basic

Energy Sciences, of the U.S. Department of Energy under Contract No. DE-AC02-05CH11231. This research used beamline 7-ID-1 (SST) and 11-BM (CMS) of the National Synchrotron Light Source II, a U.S. Department of Energy (DOE) Office of Science User Facility operated for the DOE Office of Science by Brookhaven National Laboratory under Contract No. DE-SC0012704.

The authors thank E. Gann, P. Beaucage for their contributions to RSoXS data collection and interpretation, R. Li for assistance with hard X-ray scattering measurements, and P. Ketkar for feedback and suggestions for improvement to this manuscript.

Notes

Certain commercial equipment, instruments, or materials are identified in this paper in order to specify the experimental procedure adequately. Such identification is not intended to imply recommendation or endorsement by the National Institute of Standards and Technology, nor is it intended to imply that the materials or equipment identified are necessarily the best available for the purpose.

REFERENCES

(1) Xu, Y. Chapter 19 - Hierarchical Materials. In *Modern Inorganic Synthetic Chemistry (Second Edition)*; Xu, R., Xu, Y., Eds.; Elsevier: Amsterdam, 2017; pp 545–574. https://doi.org/10.1016/B978-0-444-63591-4.00019-7.

(2) Fratzl, P.; Weinkamer, R. Nature's Hierarchical Materials. *Prog. Mater. Sci.* **2007**, *52* (8), 1263–1334. https://doi.org/10.1016/j.pmatsci.2007.06.001.

(3) Mishnaevsky, L.; Tsapatsis, M. Hierarchical Materials: Background and Perspectives. *MRS Bull.* **2016**, *41* (9), 661–664. https://doi.org/10.1557/mrs.2016.189.

(4) Lakes, R. Materials with Structural Hierarchy. *Nature* **1993**, *361* (6412), 511–515. https://doi.org/10.1038/361511a0.

(5) Xu, C.; R. Puente-Santiago, A.; Rodríguez-Padrón, D.; J. Muñoz-Batista, M.; Ariful Ahsan, M.; C. Noveron, J.; Luque, R. Nature-Inspired Hierarchical Materials for Sensing and Energy Storage Applications. *Chem. Soc. Rev.* **2021**, *50* (8), 4856–4871. https://doi.org/10.1039/C8CS00652K.

(6) Wang, Y.; Chen, J.; Li, Y.; Niu, Y.; Wang, Q.; Wang, H. Multilayered Hierarchical Polymer Composites for High Energydensity Capacitors. *J. Mater. Chem. A* **2019**, *7* (7), 2965–2980. https://doi.org/10.1039/C8TA11392K.

(7) Sun, Q.; Dai, Z.; Meng, X.; Xiao, F.-S. Porous Polymer Catalysts with Hierarchical Structures. *Chem. Soc. Rev.* **2015**, *44* (17), 6018–6034. https://doi.org/10.1039/C5CS00198F.

(8) A. Parlett, C. M.; Wilson, K.; F. Lee, A. Hierarchical Porous Materials: Catalytic Applications. *Chem. Soc. Rev.* **2013**, *42* (9), 3876–3893. https://doi.org/10.1039/C2CS35378D.

(9) Chen, L.-J.; Yang, H.-B. Construction of Stimuli-Responsive Functional Materials via Hierarchical Self-Assembly Involving Coordination Interactions. *Acc. Chem. Res.* **2018**, *51* (11), 2699–2710. https://doi.org/10.1021/acs.accounts.8b00317.

(10) Baer, E.; Hiltner, A.; Keith, H. D. Hierarchical Structure in Polymeric Materials. *Science* **1987**, *235* (4792), 1015–1022. https://doi.org/10.1126/science.3823866.

(11) Perry, S. L. Phase Separation: Bridging Polymer Physics and Biology. *Curr. Opin. Colloid Interface Sci.* **2019**, *39*, 86–97. https://doi.org/10.1016/j.cocis.2019.01.007.

(12) Van Horn, R. M.; Steffen, M. R.; O'Connor, D. Recent Progress in Block Copolymer Crystallization. *Polym. Cryst.* **2018**, *1* (4), e10039. https://doi.org/10.1002/pcr2.10039.

(13) Bates, C. M.; Bates, F. S. 50th Anniversary Perspective: Block Polymers—Pure Potential. *Macromolecules* **2017**, *50* (1), 3–22.

https://doi.org/10.1021/acs.macromol.6b02355.
(14) Polymeropoulos, G.; Zapsas, G.; Ntetsikas, K.; Bilalis, P.; Gnanou, Y.; Hadjichristidis, N. 50th Anniversary Perspective: Polymers with Complex Architectures. *Macromolecules* **2017**, *50* (4), 1253–1290. https://doi.org/10.1021/acs.macromol.6b02569.
(15) Wang, L.; Lin, J.; Zhang, X. Hierarchical Microstructures Self-Assembled from Polymer Systems. *Polymer* **2013**, *54* (14), 3427–3442. https://doi.org/10.1016/j.polymer.2013.03.054.
(16) Patel, B. B.; Diao, Y. Multiscale Assembly of Solution-Processed Organic Electronics: The Critical Roles of Confinement, Fluid Flow, and Interfaces. *Nanotechnology* **2017**, *29* (4), 044004. https://doi.org/10.1088/1361-6528/aa9d7c.
(17) Bates, F. S.; Fredrickson, G. H. Block Copolymer Thermodynamics: Theory and Experiment. *Annu. Rev. Phys. Chem.* **1990**, *41* (1), 525–557. https://doi.org/10.1146/annurev.pc.41.100190.002521.
(18) Segalman, R. A. Patterning with Block Copolymer Thin Films. *Mater. Sci. Eng. R Rep.* **2005**, *48* (6), 191–226. https://doi.org/10.1016/j.mser.2004.12.003.
(19) Luo, M.; Epps, T. H. Directed Block Copolymer Thin Film Self-Assembly: Emerging Trends in Nanopattern Fabrication. *Macromolecules* **2013**, *46* (19), 7567–7579. https://doi.org/10.1021/ma401112y.
(20) Bates, C. M.; Maher, M. J.; Janes, D. W.; Ellison, C. J.; Willson, C. G. Block Copolymer Lithography. *Macromolecules* **2014**, *47* (1), 2–12. https://doi.org/10.1021/ma401762n.
(21) Müllner, M.; Müller, A. H. E. Cylindrical Polymer Brushes – Anisotropic Building Blocks, Unimolecular Templates and Particulate Nanocarriers. *Polymer* **2016**, *98*, 389–401. https://doi.org/10.1016/j.polymer.2016.03.076.
(22) Kataoka, K.; Harada, A.; Nagasaki, Y. Block Copolymer Micelles for Drug Delivery: Design, Characterization and Biological Significance. *Adv. Drug Deliv. Rev.* **2012**, *64*, 37–48. https://doi.org/10.1016/j.addr.2012.09.013.
(23) Alvarez-Fernandez, A.; Cummins, C.; Saba, M.; Steiner, U.; Fleury, G.; Ponsinet, V.; Guldin, S. Block Copolymer Directed Metamaterials and Metasurfaces for Novel Optical Devices. *Adv. Opt. Mater.* **2021**, *9* (16), 2100175. https://doi.org/10.1002/adom.202100175.
(24) Wang, Z.; Chan, C. L. C.; Zhao, T. H.; Parker, R. M.; Vignolini, S. Recent Advances in Block Copolymer Self-Assembly for the Fabrication of Photonic Films and Pigments. *Adv. Opt. Mater.* **2021**, *9* (21), 2100519. https://doi.org/10.1002/adom.202100519.
(25) Liberman-Martin, A. L.; Chu, C. K.; Grubbs, R. H. Application of Bottlebrush Block Copolymers as Photonic Crystals. *Macromol. Rapid Commun.* **2017**, *38* (13), 1700058. https://doi.org/10.1002/marc.201700058.
(26) Pan, T.; Dutta, S.; Kamble, Y.; Patel, B. B.; Wade, M. A.; Rogers, S. A.; Diao, Y.; Guironnet, D.; Sing, C. E. Materials Design of Highly Branched Bottlebrush Polymers at the Intersection of Modeling, Synthesis, Processing, and Characterization. *Chem. Mater.* **2022**, *34* (5), 1990–2024. https://doi.org/10.1021/acs.chemmater.1c04030.
(27) Botiz, I.; Darling, S. B. Optoelectronics Using Block Copolymers. *Mater. Today* **2010**, *13* (5), 42–51. https://doi.org/10.1016/S1369-7021(10)70083-3.
(28) Bates, F. S.; Fredrickson, G. H. Block Copolymers—Designer Soft Materials. *Phys. Today* **1999**, *52* (2), 32–38. https://doi.org/10.1063/1.882522.
(29) Wan, L.; Ruiz, R.; Gao, H.; Patel, K. C.; Albrecht, T. R.; Yin, J.; Kim, J.; Cao, Y.; Lin, G. The Limits of Lamellae-Forming PS-b-PMMA Block Copolymers for Lithography. *ACS Nano* **2015**, *9* (7), 7506–7514. https://doi.org/10.1021/acsnano.5b02613.

(30) Sinturel, C.; Bates, F. S.; Hillmyer, M. A. High χ–Low N Block Polymers: How Far Can We Go? *ACS Macro Lett.* **2015**, *4* (9), 1044–1050. https://doi.org/10.1021/acsmacrolett.5b00472.

(31) Ndaya, D.; Bosire, R.; Vaidya, S.; M. Kasi, R. Molecular Engineering of Stimuli-Responsive, Functional, Side-Chain Liquid Crystalline Copolymers: Synthesis, Properties and Applications. *Polym. Chem.* **2020**, *11* (37), 5937–5954. https://doi.org/10.1039/D0PY00749H.

(32) Maher, M. J.; Bates, C. M.; Blachut, G.; Sirard, S.; Self, J. L.; Carlson, M. C.; Dean, L. M.; Cushen, J. D.; Durand, W. J.; Hayes, C. O.; Ellison, C. J.; Willson, C. G. Interfacial Design for Block Copolymer Thin Films. *Chem. Mater.* **2014**, *26* (3), 1471–1479. https://doi.org/10.1021/cm403813q.

(33) Albert, J. N. L.; Epps, T. H. Self-Assembly of Block Copolymer Thin Films. *Mater. Today* **2010**, *13* (6), 24–33. https://doi.org/10.1016/S1369-7021(10)70106-1.

(34) Feng, H.; Dolejsi, M.; Zhu, N.; Yim, S.; Loo, W.; Ma, P.; Zhou, C.; Craig, G. S. W.; Chen, W.; Wan, L.; Ruiz, R.; de Pablo, J. J.; Rowan, S. J.; Nealey, P. F. Optimized Design of Block Copolymers with Covarying Properties for Nanolithography. *Nat. Mater.* **2022**, *21* (12), 1426–1433. https://doi.org/10.1038/s41563-022-01392-1.

(35) Nakatani, R.; Takano, H.; Chandra, A.; Yoshimura, Y.; Wang, L.; Suzuki, Y.; Tanaka, Y.; Maeda, R.; Kihara, N.; Minegishi, S.; Miyagi, K.; Kasahara, Y.; Sato, H.; Seino, Y.; Azuma, T.; Yokoyama, H.; Ober, C. K.; Hayakawa, T. Perpendicular Orientation Control without Interfacial Treatment of RAFT-Synthesized High-χ Block Copolymer Thin Films with Sub-10 Nm Features Prepared via Thermal Annealing. *ACS Appl. Mater. Interfaces* **2017**, *9* (37), 31266–31278. https://doi.org/10.1021/acsami.6b16129.

(36) Yoshimura, Y.; Chandra, A.; Nabae, Y.; Hayakawa, T. Chemically Tailored High-χ Block Copolymers for Perpendicular Lamellae via Thermal Annealing. *Soft Matter* **2019**, *15* (17), 3497–3506. https://doi.org/10.1039/C9SM00128J.

(37) Verploegen, E.; Zhang, T.; Jung, Y. S.; Ross, C.; Hammond, P. T. Controlling the Morphology of Side Chain Liquid Crystalline Block Copolymer Thin Films through Variations in Liquid Crystalline Content. *Nano Lett.* **2008**, *8* (10), 3434–3440. https://doi.org/10.1021/nl802298m.

(38) Lee, C.; Ndaya, D.; Bosire, R.; Gabinet, U. R.; Sun, J.; Gopalan, P.; Kasi, R. M.; Osuji, C. O. Effects of Labile Mesogens on the Morphology of Liquid Crystalline Block Copolymers in Thin Films. *Macromolecules* **2021**, *54* (7), 3223–3231. https://doi.org/10.1021/acs.macromol.1c00100.

(39) Xie, H.-L.; Li, X.; Ren, J.; Bishop, C.; Arges, C. G.; Nealey, P. F. Controlling Domain Orientation of Liquid Crystalline Block Copolymer in Thin Films through Tuning Mesogenic Chemical Structures. *J. Polym. Sci. Part B Polym. Phys.* **2017**, *55* (6), 532–541. https://doi.org/10.1002/polb.24302.

(40) Yu, H.; Kobayashi, T.; Yang, H. Liquid-Crystalline Ordering Helps Block Copolymer Self-Assembly. *Adv. Mater.* **2011**, *23* (29), 3337–3344. https://doi.org/10.1002/adma.201101106.

(41) Qu, T.; Guan, S.; Zheng, X.; Chen, A. Perpendicularly Aligned Nanodomains on Versatile Substrates via Rapid Thermal Annealing Assisted by Liquid Crystalline Ordering in Block Copolymer Films. *Nanoscale Adv.* **2020**, *2* (4), 1523–1530. https://doi.org/10.1039/D0NA00057D.

(42) Luo, Y.; Montarnal, D.; Kim, S.; Shi, W.; Barteau, K. P.; Pester, C. W.; Hustad, P. D.; Christianson, M. D.; Fredrickson, G. H.; Kramer, E. J.; Hawker, C. J. Poly(Dimethylsiloxane-b-Methyl Methacrylate): A Promising Candidate for Sub-10 Nm Patterning. *Macromolecules* **2015**, *48* (11), 3422–3430.

https://doi.org/10.1021/acs.macromol.5b00518.
(43) Zha, W.; Han, C. D.; Lee, D. H.; Han, S. H.; Kim, J. K.; Kang, J. H.; Park, C. Origin of the Difference in Order−Disorder Transition Temperature between Polystyrene-Block-Poly(2-Vinylpyridine) and Polystyrene-Block-Poly(4-Vinylpyridine) Copolymers. *Macromolecules* **2007**, *40* (6), 2109–2119. https://doi.org/10.1021/ma062516u.
(44) Li, X.; Li, J.; Wang, C.; Liu, Y.; Deng, H. Fast Self-Assembly of Polystyrene-b-Poly(Fluoro Methacrylate) into Sub-5 Nm Microdomains for Nanopatterning Applications. *J. Mater. Chem. C* **2019**, *7* (9), 2535–2540. https://doi.org/10.1039/C8TC06480F.
(45) Wang, C.; Li, X.; Deng, H. Synthesis of a Fluoromethacrylate Hydroxystyrene Block Copolymer Capable of Rapidly Forming Sub-5 Nm Domains at Low Temperatures. *ACS Macro Lett.* **2019**, *8* (4), 368–373. https://doi.org/10.1021/acsmacrolett.9b00178.
(46) Jo, S.; Jeon, S.; Jun, T.; Park, C.; Ryu, D. Y. Fluorine-Containing Styrenic Block Copolymers toward High χ and Perpendicular Lamellae in Thin Films. *Macromolecules* **2018**, *51* (18), 7152–7159. https://doi.org/10.1021/acs.macromol.8b01325.
(47) Maeda, R.; Hayakawa, T.; Ober, C. K. Dual Mode Patterning of Fluorine-Containing Block Copolymers through Combined Top-down and Bottom-up Lithography. *Chem. Mater.* **2012**, *24* (8), 1454–1461. https://doi.org/10.1021/cm300093e.
(48) Cao, H.; Dai, L.; Liu, Y.; Li, X.; Yang, Z.; Deng, H. Methacrylic Block Copolymers Containing Liquid Crystalline and Fluorinated Side Chains Capable of Fast Formation of 4 Nm Domains. *Macromolecules* **2020**, *53* (20), 8757–8764. https://doi.org/10.1021/acs.macromol.0c00777.
(49) Busch, P.; Krishnan, S.; Paik, M.; Toombes, G. E. S.; Smilgies, D.-M.; Gruner, S. M.; Ober, C. K. Surface Induced Tilt Propagation in Thin Films of Semifluorinated Liquid Crystalline Side Chain Block Copolymers. *Macromolecules* **2007**, *40* (1), 81–89. https://doi.org/10.1021/ma061009+.
(50) Al-Hussein, M.; Séréro, Y.; Konovalov, O.; Mourran, A.; Möller, M.; de Jeu, W. H. Nanoordering of Fluorinated Side-Chain Liquid Crystalline/Amorphous Diblock Copolymers. *Macromolecules* **2005**, *38* (23), 9610–9616. https://doi.org/10.1021/ma050972x.
(51) Dong, L.; Chandra, A.; Wylie, K.; Nabae, Y.; Hayakawa, T. Tunable Thin Film Periodicities by Controlling the Orientation of Cylindrical Domains in Side Chain Liquid Crystalline Block Copolymers. *Int. J. Polym. Sci.* **2022**, *2022*, e8286518. https://doi.org/10.1155/2022/8286518.
(52) Hoyle, C. E.; Lowe, A. B.; Bowman, C. N. Thiol-Click Chemistry: A Multifaceted Toolbox for Small Molecule and Polymer Synthesis. *Chem. Soc. Rev.* **2010**, *39* (4), 1355–1387. https://doi.org/10.1039/B901979K.
(53) Muzammil, E. M.; Khan, A.; Stuparu, M. C. Post-Polymerization Modification Reactions of Poly(Glycidyl Methacrylate)s. *RSC Adv.* **2017**, *7* (88), 55874–55884. https://doi.org/10.1039/C7RA11093F.
(54) Burns, A. B.; Christie, D.; Mulhearn, W. D.; Register, R. A. Estimating the Segregation Strength of Microphase-Separated Diblock Copolymers from the Interfacial Width. *J. Polym. Sci. Part B Polym. Phys.* **2019**, *57* (14), 932–940. https://doi.org/10.1002/polb.24848.
(55) Hamley, I. W.; Castelletto, V. Small-Angle Scattering of Block Copolymers: In the Melt, Solution and Crystal States. *Prog. Polym. Sci.* **2004**, *29* (9), 909–948. https://doi.org/10.1016/j.progpolymsci.2004.06.001.
(56) Brown, E. N.; Rae, P. J.; Dattelbaum, D. M.; Clausen, B.; Brown, D. W. In-Situ Measurement of Crystalline Lattice Strains in Polytetrafluoroethylene. *Exp. Mech.* **2008**, *48* (1), 119–131. https://doi.org/10.1007/s11340-007-9075-3.

(57) Snyder, C. R.; Kline, R. J.; DeLongchamp, D. M.; Nieuwendaal, R. C.; Richter, L. J.; Heeney, M.; McCulloch, I. Classification of Semiconducting Polymeric Mesophases to Optimize Device Postprocessing. *J. Polym. Sci. Part B Polym. Phys.* **2015**, *53* (23), 1641–1653. https://doi.org/10.1002/polb.23801.

(58) Wunderlich, B. A Classification of Molecules, Phases, and Transitions as Recognized by Thermal Analysis. *Thermochim. Acta* **1999**, *340–341*, 37–52. https://doi.org/10.1016/S0040-6031(99)00252-X.

(59) Toda, A. Heating Rate Dependence of Melting Peak Temperature Examined by DSC of Heat Flux Type. *J. Therm. Anal. Calorim.* **2016**, *123* (3), 1795–1808. https://doi.org/10.1007/s10973-015-4603-3.

(60) Kim, S.; Bates, C. M.; Thio, A.; Cushen, J. D.; Ellison, C. J.; Willson, C. G.; Bates, F. S. Consequences of Surface Neutralization in Diblock Copolymer Thin Films. *ACS Nano* **2013**, *7* (11), 9905–9919. https://doi.org/10.1021/nn403616r.

(61) Harris, M.; Appel, G.; Ade, H. Surface Morphology of Annealed Polystyrene and Poly(Methyl Methacrylate) Thin Film Blends and Bilayers. *Macromolecules* **2003**, *36* (9), 3307–3314. https://doi.org/10.1021/ma0257043.

(62) Collins, B. A.; Gann, E. Resonant Soft X-ray Scattering in Polymer Science. *J. Polym. Sci.* **2022**, *60* (7), 1199–1243. https://doi.org/10.1002/pol.20210414.

(63) Watts, B. Calculation of the Kramers-Kronig Transform of X-Ray Spectra by a Piecewise Laurent Polynomial Method. *Opt. Express* **2014**, *22* (19), 23628–23639. https://doi.org/10.1364/OE.22.023628.

(64) Mukherjee, S.; Streit, J. K.; Gann, E.; Saurabh, K.; Sunday, D. F.; Krishnamurthy, A.; Ganapathysubramanian, B.; Richter, L. J.; Vaia, R. A.; DeLongchamp, D. M. Polarized X-Ray Scattering Measures Molecular Orientation in Polymer-Grafted Nanoparticles. *Nat. Commun.* **2021**, *12* (1), 4896. https://doi.org/10.1038/s41467-021-25176-4.

(65) Saurabh, K.; Dudenas, P. J.; Gann, E.; Reynolds, V. G.; Mukherjee, S.; Sunday, D.; Martin, T. B.; Beaucage, P. A.; Chabinyc, M. L.; DeLongchamp, D. M.; Krishnamurthy, A.; Ganapathysubramanian, B. CyRSoXS: A GPU-Accelerated Virtual Instrument for Polarized Resonant Soft X-Ray Scattering. *J. Appl. Crystallogr.* **2023**, *56* (3), 868–883. https://doi.org/10.1107/S1600576723002790.

(66) Müller-Buschbaum, P. A Basic Introduction to Grazing Incidence Small-Angle X-Ray Scattering. In *Applications of Synchrotron Light to Scattering and Diffraction in Materials and Life Sciences*; Gomez, M., Nogales, A., Garcia-Gutierrez, M. C., Ezquerra, T. A., Eds.; Lecture Notes in Physics; Springer Berlin Heidelberg: Berlin, Heidelberg, 2009; Vol. 776, pp 61–89. https://doi.org/10.1007/978-3-540-95968-7_3.

(67) Smilgies, D.-M. GISAXS: A Versatile Tool to Assess Structure and Self-Assembly Kinetics in Block Copolymer Thin Films. *J. Polym. Sci.* **2022**, *60* (7), 1023–1041. https://doi.org/10.1002/pol.20210244.

(68) Busch, P.; Rauscher, M.; Smilgies, D.-M.; Posselt, D.; Papadakis, C. M. Grazing-Incidence Small-Angle X-Ray Scattering from Thin Polymer Films with Lamellar Structures – the Scattering Cross Section in the Distorted-Wave Born Approximation. *J. Appl. Crystallogr.* **2006**, *39* (3), 433–442. https://doi.org/10.1107/S0021889806012337.

(69) Page, K. A.; Kusoglu, A.; Stafford, C. M.; Kim, S.; Kline, R. J.; Weber, A. Z. Confinement-Driven Increase in Ionomer Thin-Film Modulus. *Nano Lett.* **2014**, *14* (5), 2299–2304. https://doi.org/10.1021/nl501233g.

(70) Baker, J. L.; Jimison, L. H.; Mannsfeld, S.; Volkman, S.; Yin, S.; Subramanian, V.; Salleo, A.; Alivisatos, A. P.; Toney, M. F. Quantification of Thin Film Crystallographic Orientation Using X-Ray Diffraction with an Area Detector. *Langmuir* **2010**, *26* (11), 9146–9151. https://doi.org/10.1021/la904840q.

(71) Ilavsky, J. Nika: Software for Two-Dimensional Data Reduction. *J. Appl. Crystallogr.* **2012**, *45* (2), 324–328. https://doi.org/10.1107/S0021889812004037.
(72) Jiang, Z. GIXSGUI: A MATLAB Toolbox for Grazing-Incidence X-Ray Scattering Data Visualization and Reduction, and Indexing of Buried Three-Dimensional Periodic Nanostructured Films. *J. Appl. Crystallogr.* **2015**, *48* (3), 917–926. https://doi.org/10.1107/S1600576715004434.
(73) Ren, J.; Ocola, L. E.; Divan, R.; Czaplewski, D. A.; Segal-Peretz, T.; Xiong, S.; Kline, R. J.; Arges, C. G.; Nealey, P. F. Post-Directed-Self-Assembly Membrane Fabrication for in Situ Analysis of Block Copolymer Structures. *Nanotechnology* **2016**, *27* (43), 435303. https://doi.org/10.1088/0957-4484/27/43/435303.
(74) Gann, E.; Crofts, T.; Holland, G.; Beaucage, P.; McAfee, T.; Kline, R. J.; Collins, B. A.; McNeill, C. R.; Fischer, D. A.; DeLongchamp, D. M. A NIST Facility for Resonant Soft X-Ray Scattering Measuring Nano-Scale Soft Matter Structure at NSLS-II. *J. Phys. Condens. Matter* **2021**, *33* (16), 164001. https://doi.org/10.1088/1361-648X/abdffb.
(75) Beaucage, P. PyHyperScattering Release 0.1.10, 2022. https://github.com/usnist-gov/PyHyperScattering (accessed 2023-01-10).
(76) Schawe, J. E. K.; Pogatscher, S. Material Characterization by Fast Scanning Calorimetry: Practice and Applications. In *Fast Scanning Calorimetry*; Schick, C., Mathot, V., Eds.; Springer International Publishing: Cham, 2016; pp 3–80. https://doi.org/10.1007/978-3-319-31329-0_1.
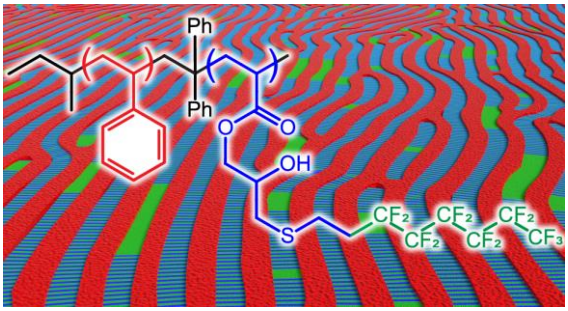
For Table of Contents Only